OTC-26112-MS

Truncated Multi-Gaussian Pore-Throat-Size Decomposition and a New Universal J-Function for Rock Characterization of Complex Carbonate Reservoirs

Ferreira, F.C., Booth, R., Oliveira, R., Boyd, A., SPE, Schlumberger, Bize-Forest, N., and Wahanik, H., Schlumberger

This paper was prepared for presentation at the Offshore Technology Conference Brasil held in Rio de Janeiro, Brazil, 27–29 October 2015.

Abstract

Rock-pore-space geometry and network topology have a great impact on dynamic reservoir characteristics, in particular on capillary pressure and relative permeability curves. In complex and heterogeneous carbonate reservoirs, the rock-pore-throat-size distribution is typically multimodal and its decomposition may be an important concept for reservoir characterization and simulation. Our objectives are to enhance current dynamic reservoir characterization processes and to assess the corresponding improved fidelity of reservoir simulation.

We propose an innovative and precise mathematical formulation of the pore-throat-size distribution as a truncated multi-Gaussian decomposition, matching its parameters to experimental data through both direct and inverse approaches. Based on the above technique we also propose a new multi-Gaussian universal J^{**}-function and a new dynamic reservoir-rock-typing index. We also prepare a comprehensive sensitivity study on the impact of multimodal dynamic reservoir characteristics on oil recovery results. For this sensitivity study, we use a synthetic dual-porosity carbonate-reservoir simulation model, incorporating the concept of the proposed universal J^{**}-function to derive the corresponding dynamic reservoir properties.

We applied the multi-Gaussian decomposition to the experimental mercury-injection-capillary-pressure (MICP) data from the Worldwide Rock Catalog (WWRC), provided by a joint-industry project (Core Lab, 2014). We used the multi-Gaussian universal J^{**}-function to demonstrate the excellent results of such decomposition. These results showed large variability of multimodality for both clastic and carbonate rocks. We also found correlations between decomposition parameters, rock properties and rock textures. Considering the truncation of the pore-throat-size distribution proved to be important to model the physical and experimental limits of the data. The results of the sensitivity study showed a significant impact of multimodality variability on oil in place and reserves estimates for improved oil recovery (IOR) and enhanced oil recovery (EOR) processes in complex carbonate reservoirs, such as the ones found in the Brazilian Pre-Salt. It also showed the importance of considering pore-throat-size multimodality when deriving dynamic reservoir properties from capillary pressure and relative permeability experiments. In complex carbonate reservoirs under IOR/EOR, overlooking the rock-pore-space geometry and network

topology may result in significant deviations in the quality of reservoir characterization and simulation results. In this context, proper multi-Gaussian decomposition and the introduction of a new multi-Gaussian universal J^{**}-function are therefore crucial for carbonate reservoir simulations.

The proposed truncated multi-Gaussian pore-throat-size decomposition presents significant additional benefits when compared to Thomeer's method. It also improves dynamic-reservoir-rock-typing and reservoir simulation processes. The new universal J^{**}-function can be used to reconstruct capillary pressure curves from the information provided by multi-Gaussian pore-throat-size decomposition. Therefore, the new concepts presented in this paper have a clear potential to enhance the simulation of IOR and EOR in complex carbonate and clastic reservoirs.

Introduction

This paper focuses on the dynamic reservoir characterization of multiphase transport and saturation phenomena in complex porous media. The main corresponding capillary effects are wettability; capillary pressure and relative permeability curves; end-point saturations; and hysteresis. Such capillary effects are especially important for the simulation of reservoirs under IOR / EOR processes or producing under gas or water natural drives. This paper is a further development of the study presented by Ferreira et al. (2015), where they have shown the importance of hydraulic tortuosity and corresponding pore-throat-size variability to the dynamic characterization of complex carbonate reservoirs. This study extends their approach to consider multimodal rocks.

Accurate static and dynamic reservoir characterization are key requirements for reservoir management and simulation. The characterization workflows rely on the integration of data and understanding across multiple scales and domains - from the pore scale to the reservoir scale and through the petrophysics, reservoir engineering, geology and geophysics domains. Reservoir characterization methodologies estimate rock properties from core, well log and seismic measurements, and then distribute such properties throughout the reservoir by associating geological facies to petrophysical facies, and identifying static and dynamic reservoir-rock types (Cosentino, 1992 and Jerry Lucia, 1999).

Ferreira et al. (2015) proposed a new dynamic reservoir-rock-typing index (RQI*) using absolute permeability, porosity and hydraulic tortuosity data, derived from mercury-injection-capillary-pressure (MICP) experiments. RQI* is based on the following modified Kozeny equation:

$$\langle r_{\text{throat}}^2 \rangle = 8 \frac{k \tau_h}{\phi_e}, \tag{1}$$

where ϕ_e is the effective porosity, k is the absolute permeability, τ_h is the hydraulic tortuosity and $\langle r_{\text{throat}}^2 \rangle$ is the average pore-throat squared radius of the rock. RQI* is then defined by:

$$\text{RQI}^* = \sqrt{k\tau_h / \phi_e} = \sqrt{\langle r_{\text{throat}}^2 \rangle / 8}\,. \tag{2}$$

Ferreira et al. (2015) showed that RQI* has a much stronger correlation with pore-space geometry when compared with Winland R35, reservoir-quality (RQI) and flow-zone (FZI) indexes. Therefore, RQI* presents a clear potential to enhance the dynamic rock typing and the upscaling of capillary effects for reservoir simulation of IOR / EOR in complex carbonate rocks. They also showed that dielectric measurements in both core and well log scales have significant potential for deriving electrical and hydraulic tortuosity properties, consequently enabling RQI* upscaling.

The RQI* definition (Eq. (2)) highlights the correspondence between RQI* and the rock-pore-throat-size distribution. Therefore, RQI* links absolute permeability and effective porosity to pore-space geometry and connects the pore and the core scales. Eq. (1) shows that rocks with the same ratio k/ϕ_e may have very different pore-throat sizes, if the hydraulic tortuosity τ_h is different from rock to rock.

We may better understand the importance of rock-pore-throat-size distribution for the characterization of capillary effects by thinking of a fluid particle inside a pore. It can only interact with other nearby fluid particles or with the pore walls. The consequences are clear by examining the Young-Laplace-Washburn (1921) equation for the drainage capillary pressure P_c:

$$P_c = \frac{2\gamma \cos(\theta)}{r_{\text{throat}}}. \tag{3}$$

In the equation above, the fluids' interfacial tension γ represents the fluid-fluid interactions, the contact angle θ represents the fluid-rock interactions, and the pore-throat radius r_{throat} represents the pore space geometry. Therefore, pore-scale properties entirely govern the capillary effects: there is no direct reference to bulk properties like absolute permeability or effective porosity in Eq. (3). We may use such bulk properties to correlate pore-scale average properties to bulk measurements, as exemplified by Eq. (1). The characterization of capillary effects like relative permeability, saturation distribution, wettability and hysteresis may also require other relevant pore-scale geometry properties as pore-body and pore-throat-size distribution; percolation path and threshold; pore connectivity and pore shape. Rock mineralogy, fluid characteristics and their interactions under reservoir conditions complete the required scenario for a proper dynamic characterization.

In the industry, R_{35} and R_d are considered key points for drainage capillary pressure curve characterization. They are also relevant points for relative permeability and end-point saturations. R_d is the pore-throat size corresponding to the entry capillary pressure, the highest pressure before the non-wetting fluid first enters the rock. R_{35} corresponds to the capillary pressure when the non-wetting-fluid saturation reaches 35%. **Figure 1** shows the position of such points on a capillary pressure curve. R_{35} and R_d may be calculated using Eq. (3). Ferreira et al. (2015) showed that RQI* presents excellent correlation with both R_{35} and R_d, whereas Winland R35 index, reservoir quality index (RQI) and flow-zone indicator (FZI) all show a fair correlation with R_{35}, but a poor correlation with R_d.

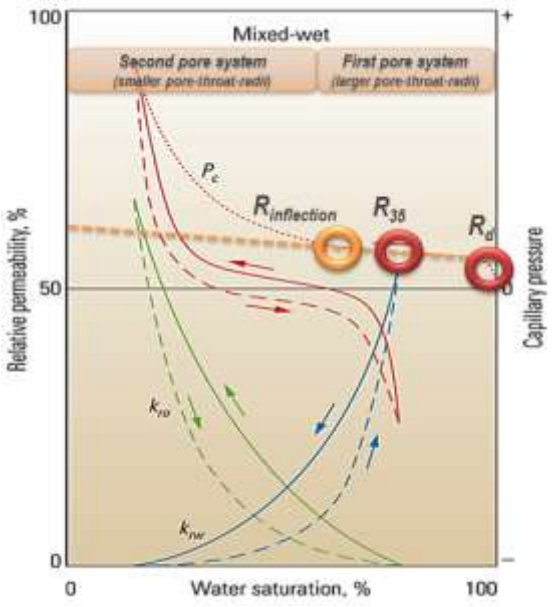

Figure 1 - Drainage capillary pressure key points (modified over the original picture from Schlumberger Oilfield Review, Summer 2007, pg. 50)

For unimodal pore-throat-size rocks, R_{35} and R_d may be enough for a good capillary pressure curve characterization. Nevertheless, in the case of multimodal rocks, including most carbonates, R_{35} and R_d are typically associated only with the pore system corresponding to the larger-pore-throat radii, from now on simply referred to as the first pore system. Therefore, multimodal pore-throat-size distribution analysis is then required to complement the RQI* analysis with the characterization of the pore systems corresponding to smaller-pore-throat radii, from now on referred to as the second or third pore systems. Similarly, the Gaussian component

corresponding to the larger-pore-throat radii is simply referred to as the first Gaussian component, and so on for the components with smaller-pore-throat radii.

Skalinski et al. (2006) have proposed a hyperbolic tangent curve fitting method to extend the capillary pressure characterization. Such method defines the pore-throat radius $R_{\text{inflection}}$ corresponding to the curve inflection point and the derivative at such point as shown in Figure 1. The method proposed by Skalinski may qualitatively distinguish unimodal from multimodal rocks, but it does not include a multimodal decomposition approach. Therefore, it does not properly characterize the second or third pore systems of a multimodal rock.

Thomeer (1960) has proposed a widely accepted method for multimodal-pore-system decomposition, by fitting data from MICP experiments to hyperbolas, given by:

$$\frac{B_v}{B_\infty} = \exp\left(-G/\log_{10}(P_c/P_d)\right), \tag{4}$$

where B_v is the volume fraction of the injected mercury to the total sample's bulk volume at a mercury-injection pressure P_c, B_∞ is the bulk volume percentage occupied by mercury at the maximum applied pressure, G is the pore geometrical factor and P_d is the displacement pressure required to first intrude mercury into the largest pore-throat. A single pore system may be represented by one Thomeer hyperbola and is characterized by three parameters: P_d, B_∞ and G. The pore geometrical factor G corresponds to the uniformity (low G) or non-uniformity (high G) of the pore-throat sizes. Thomeer hyperbolas can be combined or superposed to quantify complex multimodal pore systems. Such method is extensively covered by Clerke and Martin (2004) and Clerke et al. (2008).

Xu and Torres-Verdín (2013) introduced a bi-Gaussian density function to characterize logarithmic rock-pore-throat-radius distributions from MICP experiments. Such a bi-Gaussian model generates five independent attributes, providing a quantitative basis for petrophysical modeling and rock typing. These attributes are the volume fraction for the first Gaussian component; the mean value of the logarithmic pore-throat radius for each Gaussian component; and the corresponding standard deviations of the logarithmic pore-throat radius.

Xu and Torres-Verdín (2013) found good correlations between some of these attributes and their associated petrophysical properties for a specific field case. Both absolute permeability and end-point gas relative permeability showed good correlation with the mean value of the first Gaussian mode. Likewise, the irreducible water saturation (from capillary pressure) showed a good correlation with the mean value of the pore-throat radius for the second Gaussian component, and the critical water saturation (from relative permeability) showed a good correlation with the fraction of the pore volume connected to the second Gaussian component. They also proposed the use of the parameters of the bi-Gaussian decomposition for rock typing by clustering analysis.

In this paper, we further develop Xu and Torres-Verdín (2013) work to propose a precise mathematical multi-Gaussian decomposition of the pore-throat-size distribution considering the truncation of the capillary pressure data. We match its parameters to experimental data through both direct and inverse approaches. Considering the truncation of the pore-throat-size distribution by the physical and experimental limits of the data significantly improved the matching results. Both clastic and carbonate rocks in the WWRC showed large variability of the decomposition parameters and multimodality. Similar to Xu and Torres-Verdín (2013), we also found interesting correlations between decomposition parameters and rock properties.

Another important concept related to capillary pressure, pore geometry parameters, rock typing and rock-typing indexes is the J-function introduced by Leverett (1941):

$$J = \frac{P_c}{\gamma \cos(\theta)} \sqrt{\frac{k}{\phi_e}} \tag{5}$$

The Leverett J-function is a capillary pressure normalization function originally derived from dimension analysis. It typically reduces the scattering of the capillary curves. Several workflows and software tools for reservoir characterization and simulation apply the Leverett J-function. In a typical workflow, individual capillary pressure curves are normalized, then the resulting J-functions are averaged and finally rescaled according to the individual k/ϕ_e ratio to rebuild the resulting capillary pressure curves. However, its use for characterizing complex, multimodal carbonates has been frequently challenged (Clerke et al. (2008)). We too consider the use of the Leverett J-function inappropriate for such rocks.

El-Khatib (1995) proposed a modified J^*-function by including the hydraulic tortuosity parameter τ_h. Ferreira et al. (2015) have further modified the J^*-function to obtain:

$$J^*(S_w^*) = \frac{P_c}{\gamma \cos(\theta)} \sqrt{\frac{k\tau_h}{\phi_e}} = \frac{2}{r_{\text{throat}}} \sqrt{\frac{k\tau_h}{\phi_e}} = \frac{2\text{RQI}^*}{r_{\text{throat}}}, \tag{6}$$

showing that the J^*-function is directly proportional to the ratio between RQI^* and the corresponding r_{throat}. By knowing RQI^*, we may then obtain drainage capillary pressure curves combining Eq. (6) to the distribution of r_{throat} as a function of the normalized wetting-fluid saturation S_{w}^* defined as:

$$S_{\text{w}}^* = \frac{(S_{\text{wmax}} - S_{\text{w}})}{(S_{\text{wmax}} - S_{\text{wmin}})}, \tag{7}$$

where S_w is the wetting phase saturation (in MICP is the air saturation), S_{wmax} and $S_{w\,min}$ are the maximum and minimum saturation reached during the drainage experiment. Usually $S_{\text{wmax}} = 1$.

The El-Khatib (1995) J^*-function has not been extensively used, mainly because its additional parameter τ_h did not have a correspondent well log measurement to enable its upscaling. However, Ferreira et al. (2015) recently showed that dielectric measurements in both core and well log scales have a significant potential for deriving electrical and hydraulic tortuosity properties.

The El-Khatib (1995) J^*-function is not universal; it still requires an averaging process. From Eq. (6), we may infer that J^* is normalized by RQI^* and different rocks with different RQI^* may present the same J^* curves. Nevertheless, the J^* formulation does not account for different degrees of rock-sorting quality, which corresponds to the standard deviation of the pore-throat-size distribution. It also does not support multimodal rock modeling. Therefore, the J^* curves may still not be coincident. See **Figure 5** (later in this paper) for examples where J^* curves are different from each other.

In this paper, based on the truncated multi-Gaussian decomposition of the pore-throat-size distribution, we also propose a new multi-Gaussian universal J^{**}-function. It can be used to validate the results of such a decomposition and to reconstruct capillary pressure curves from the decomposition parameters.

We foresee the application of the proposed multi-Gaussian pore-throat-size decomposition and the new multi-Gaussian universal J^{**}-function to complex reservoir rocks such as the Pre-Salt mixed-wet carbonates in Brazil, with planned CO2 injection / WAG processes (Pizarro and Branco, 2012). Indeed, microbial and travertine fabrics dominate the Pre-Salt carbonate rocks in Brazil and show a high degree of vertical and horizontal heterogeneity resulting from their genesis and diagenesis processes. Matrix dissolution, which creates vugs, and geothermal cementation that closes the pore space, have a large impact on the multimodality of these rocks, resulting in macro, meso and micro-pore systems.

Any dynamic reservoir characterization methodology is incomplete if laboratory core measurements cannot be upscaled to the wellbore and reservoir scales. For example, current rock-typing indexes use effective porosity and absolute permeability. Porosity measurements from well logs are relatively straightforward. On the other hand, absolute permeability upscaling requires correlations with effective porosity and other well logs, such as the nuclear magnetic resonance (NMR) log. Specific correlations and neural-network techniques may replace missing measurements to some extent. Therefore, we should also identify well log measurements and techniques, which may enable the upscaling of multi-Gaussian parameters.

Some well log measurements are useful for identifying multi-modal pore systems typically seen in carbonate formations, such as NMR, borehole images and sonic logs. NMR T2 distributions are routinely used as a proxy for MICP and are hence useful for porosity partitioning (Hassal et al, 2004). Electrical borehole image logs are also excellent for identifying vuggy porosity (Ramakrishnan et al, 2001) based on thresh-holding histograms of conductivity. Acoustic borehole image logs are similarly analyzed by thresh-holding amplitude histograms (Bize-Forest et al, 2014). Prior to the introduction of NMR and borehole image logs, sonic logs were traditionally used to indicate secondary porosity, using the deficit between sonic porosity and density-neutron porosity based on the concept that spherical, vuggy porosity is less compressible than inter-granular matrix porosity and/or intra-granular micro porosity (Brie et al, 1985). New developments in dielectric log interpretation and 2D-NMR analysis are leading to improved (Souza et al, 2013) textural analysis in carbonates for determining electric tortuosity properties, which may correlate with hydraulic tortuosity and the average pore-throat squared radius $\langle r_{\mathrm{throat}}^2 \rangle$ of the multimodal rock (Ferreira et al., 2015).

Based on the new index RQI^*, on the multi-Gaussian pore-throat-size decomposition, on the proposed J^{**}-function and on the corresponding dynamic reservoir properties, we also prepare a comprehensive sensitivity study on the impact of variability of multi-modal parameters on oil recovery results, using a synthetic carbonate-reservoir simulation model.

Truncated Multi-Gaussian Pore-Throat-Size Decomposition

In intrusion MICP experiments, injected-mercury incremental volumes are associated with the corresponding increments on injection pressure. We may then use the Young-Laplace-Washburn equation (3) to convert from the drainage capillary pressure domain (P_c) to the pore-throat-size domain (r_{throat}). Such pore-throat-radii are usually distributed through several orders of magnitude. For this reason, the logarithmic pore-throat-radius $\ln(r_{\mathrm{throat}})$ is generally used. By knowing the porous volume of the sample to the wetting fluid (air), we also may convert the injected-mercury cumulative volume to wetting-fluid saturations. We may finally use Eq. (7) to obtain a wetting-fluid normalized saturation S_w^*. The resulting S_w^* is then a function of the logarithmic pore-throat-radius $\ln(r_{\mathrm{throat}})$. The corresponding curve is analogous to a cumulative distribution function (CDF) of $\ln(r_{\mathrm{throat}})$. However, the saturation S_w^* may not directly correspond to the cumulative distribution frequency of $\ln(r_{\mathrm{throat}})$, because S_w^* is volume weighted, and because large-size pore bodies (e.g. isolated vugs) may be connected through pore throats

with a much smaller radius (known as the pore-shielding effect). Nevertheless, for practical purposes we may define the pore-throat-radius cumulative distribution as the normalized saturation obtained when the applied pressure is sufficient to allow injection of mercury through any pore throat with radius greater than (r_{throat}). With this definition, the corresponding pore-throat-radius probability-density function (PDF) may be represented by:

$$f\big(\ln(r_{\text{throat}})\big) = \frac{\mathrm{d}S_w^*}{\mathrm{d}\big(\ln(r_{\text{throat}})\big)}. \tag{8}$$

Simple unimodal rocks usually present a Gaussian distribution of $\ln(r_{\text{throat}})$ based on S_w^*, which is by definition equivalent to a lognormal distribution of r_{throat}. Therefore, the PDF of $\ln(r_{\text{throat}})$ might be represented by:

$$\frac{\mathrm{d}S_w^*}{\mathrm{d}\big(\ln(r_{\text{throat}})\big)} = \frac{1}{\sigma\sqrt{2\pi}} e^{\frac{-(\ln(r_{\text{throat}})-\mu)^2}{2\sigma^2}}, \tag{9}$$

where μ is the mean and σ is the standard deviation of the $\ln(r_{\text{throat}})$ distribution.

For ease of notation we also define

$$r_{\text{mode}} = e^{\mu}, \tag{10}$$

so that r_{mode} is the pore-throat-radius corresponding to the mode value of the PDF for $\ln(r_{\text{throat}})$.

By integrating Eq. (9) up to $\ln(r_{\text{throat}})$ we obtain S_w^* as a function of the lognormal cumulative-distribution function (CDF):

$$S_w^*(r_{\text{throat}}) = \frac{1}{2}\,\text{erfc}\left(\frac{\ln(r_{\text{mode}}/r_{\text{throat}})}{\sqrt{2}\sigma}\right). \tag{11}$$

Abramowitz and Stegun (1972) and Ren and Mackenzie (2007) present useful approximations to the complementary error function erfc.

The assumption that Eq. (8) represents the PDF of $\ln(r_{\text{throat}})$ is indeed very useful, allowing to rebuild S_w^* from the parameters of the Gaussian distribution of $\ln(r_{\text{throat}})$, as shown by Eq. (11).

We further expand Xu and Torres-Verdín (2013) theoretical approach to consider the truncation of the capillary pressure data. Such truncations may result either from experimental limitations or from the geological imprint of the rocks, whatever happens first. Maximum MICP pressure controls the minimum pore-throat-radius r_{min} while minimum pressure delimits the maximum pore-throat-radius r_d. On the other hand, if the MICP experiment broadly covers both high and low-pressure ranges, then r_{min} and r_d are defined by genesis and diagenesis processes. From the saturation perspective, r_{min} corresponds to S_{wmin} while r_d corresponds to S_{wmax}. If such limits are natural then the PDF is complete, otherwise it is experimentally limited. Our approach allows extending such experimental limits to the natural limits, if proper correlations are available. Considering the truncation of the PDF proved to be crucial to reach a proper and more general fit. It is also consistent with Thomeer's approach (Thomeer, 1960), which includes the entry capillary pressure P_d as an important parameter.

Therefore, we redefine Eq. (11) as:

$$\zeta(r_{\text{throat}}) = \frac{1}{2}\ \text{erfc}\left(\frac{\ln(r_{\text{mode}}/r_{\text{throat}})}{\sqrt{2}\sigma}\right), \tag{12}$$

to obtain the following equation for S_w^* as a function of the truncated multi-Gaussian pore-throat-size decomposition:

$$S_w^*(r_{\text{throat}}) = \frac{\zeta(r_{\text{throat}}) - \zeta(r_{\text{min}})}{\zeta(r_{\text{d}}) - \zeta(r_{\text{min}})}\ . \tag{13}$$

Eq. (13) is only valid for a single Gaussian distribution. Saturation is a volume-averaged property. Therefore, for a multi-Gaussian rock with n pore systems, $S_w^*(r_{\text{throat}})$ is the result of the volumetric averaging of each single-Gaussian normalized wetting-fluid saturation:

$$S_w^*(r_{\text{throat}}) = \sum_{j=1}^{n} x_j . S_{wj}^*(r_{\text{throat}})\ , \tag{14}$$

with:

$$S_{wj}^*(r_{\text{throat}}) = \frac{\zeta_j(r_{\text{throat}}) - \zeta_j(r_{\text{min}\,j})}{\zeta_j(r_{\text{d}\,j}) - \zeta_j(r_{\text{min}\,j})}\ , \tag{15}$$

where x_j are the volumetric fractions and ζ_j are the saturation functions for each Gaussian distribution, which are defined by the mode values $r_{mode\,j}$ of the corresponding logarithmic pore-throat-radius distribution, the logarithmic standard deviations σ_j , the maximum $r_{d\,j}$ and the minimum pore-throat-radii $r_{min\,j}$. Furthermore, the saturation function $\zeta_j(r_{\text{throat}})$ may vary from 0 to 1, and it monotonously increases with respect to r_{throat}. Of course, we also require that $\sum_{j=1}^{n} x_j = 1$.

Eqs. (14) and (15) show the linear relationship between $S_w^*(r_{\text{throat}})$ and the saturation functions $\zeta_j(r_{\text{throat}})$. Such a linear relationship may improve drainage capillary pressure upscaling processes and the building of a saturation-height-model (SHM).

Usually, we may properly fit most of the multimodal rocks by using a bi-Gaussian distribution. Only a small fraction of the samples may require a tri-Gaussian distribution. A maximum of nine independent parameters are required for bi-Gaussian cases. By convention, the first Gaussian component corresponds to the larger pore-throat radii and is represented by the index $j = 1$.

In the real world, it may be difficult to determine r_{d2} or $r_{min\,1}$, as both may be masked by the opposite superposed Gaussian distribution. Such parameters may be used to achieve a better fit of the data, but in most of the cases, it is reasonable to assume that $r_{d2} \cong r_{d1} = r_d$ and $r_{min\,1} \cong r_{min\,2} = r_{min}$. Consequently, for a bi-Gaussian distribution we have:

$$S_w^*(r_{\text{throat}}) = x_1 \frac{\zeta_1(r_{\text{throat}}) - \zeta_1(r_{min})}{\zeta_1(r_d) - \zeta_1(r_{min})} + \ (1 - x_1) \frac{\zeta_2(r_{\text{throat}}) - \zeta_2(r_{min})}{\zeta_2(r_d) - \zeta_2(r_{min})}\,. \tag{16}$$

Therefore, only seven independent parameters are required: $r_{mode\,1}$ and $r_{mode\,2}$; σ_1 and σ_2; r_d and r_{min}; and x_1. Nevertheless, r_d and r_{min} can be directly determined from the MICP experiment. Consequently, only five adjusting parameters are required (see **Figure 2a** and **Figure 2b**).

In several cases, $r_{min} \ll r_{\text{mode }1}$ and $r_d \gg r_{\text{mode }2}$. As a guide, if $\ln(r_{\text{mode }2}/r_{\text{d}})/\left(\sqrt{2}\sigma_2\right) \leq -2$ then $\zeta_2(r_d) \cong 1$. Similarly, if $\ln(r_{\text{mode }1}/r_{\text{min}})/\left(\sqrt{2}\sigma_1\right) \geq 2$ then $\zeta_1(r_{min}) \cong 0$. In these cases

$$S_w^*(r_{\text{throat}}) = x_1 \frac{\zeta_1(r_{\text{throat}})}{\zeta_1(r_d)} + (1 - x_1) \frac{\zeta_2(r_{\text{throat}}) - \zeta_2(r_{min})}{1 - \zeta_2(r_{min})}. \tag{17}$$

According to Eq. (2), the proposed RQI* index is a function of the average pore-throat squared radius $\langle r_{\text{throat}}^2 \rangle$. The later may be calculated as a function of the single Gaussian decomposition parameters from Eq. (9), carrying out the following indefinite integration:

$$\langle r_{\text{throat}}^2 \rangle = \int r_{\text{throat}}^2 . \, \text{d}S_w^* = \int \frac{\text{e}^{2\ln(r_{\text{throat}})}}{\sigma\sqrt{2\pi}} e^{\frac{-(\ln(r_{\text{throat}}) - \mu)^2}{2\sigma^2}} . \, \text{d}\left(\ln(r_{\text{throat}})\right) \tag{18}$$

$$= -\frac{1}{2} e^{2(\mu+\sigma^2)} \text{erf}\left(\frac{\mu + 2\sigma^2 - \ln(r_{\text{throat}})}{\sqrt{2}\sigma}\right).$$

For a truncated single Gaussian distribution, $\langle r_{\text{throat}}^2 \rangle$ is obtained by definite integration of Eq. (18) between $\ln(r_{\text{min}})$ and $\ln(r_{\text{d}})$, divided by the ζ (or CDF) difference corresponding to the finite support of the PDF:

$$\langle r_{\text{throat}}^2 \rangle = -\frac{1}{2} \frac{e^{2(\mu+\sigma^2)} \text{erf}\left(\frac{\mu + 2\sigma^2 - \ln(r_{\text{throat}})}{\sqrt{2}\sigma}\right)\Big]_{\ln(r_{\text{min}})}^{\ln(r_{\text{d}})}}{\zeta(r_{\text{d}}) - \zeta(r_{\text{min}})} \tag{19}$$

$$= r_{\text{mode}}^2 e^{2\sigma^2} \frac{\left(\text{erfc}\left(\frac{\ln(r_{\text{mode}}/r_{\text{d}}) + 2\sigma^2}{\sqrt{2}\sigma}\right) - \text{erfc}\left(\frac{\ln(r_{\text{mode}}/r_{\text{min}}) + 2\sigma^2}{\sqrt{2}\sigma}\right)\right)}{\text{erfc}\left(\frac{\ln(r_{\text{mode}}/r_{\text{d}})}{\sqrt{2}\sigma}\right) - \text{erfc}\left(\frac{\ln(r_{\text{mode}}/r_{\text{min}})}{\sqrt{2}\sigma}\right)}.$$

We may write Eq. (19) in the more concise form:

$$\langle r_{\text{throat}}^2 \rangle = r_{\text{mode}}^2 e^{2\sigma^2} \frac{\zeta\left(r_{\text{d}} e^{-2\sigma^2}\right) - \zeta\left(r_{\text{min}} e^{-2\sigma^2}\right)}{\zeta(r_{\text{d}}) - \zeta(r_{\text{min}})}, \tag{20}$$

where the term $\zeta(r_{\text{d}}) - \zeta(r_{\text{min}})$ accounts for the truncated average normalization.

For a pore-throat-radius multi-Gaussian distribution, by definition we have:

$$\langle r_{\text{throat}}^2 \rangle = \sum_{i=1}^{n} \langle r_{\text{throat i}}^2 \rangle . \, x_i , \tag{21}$$

and consequently

$$\text{RQI}^{*2} = \sum_{i=1}^{n} RQI_i^{*2} . \, x_i . \tag{22}$$

For the particular case of a bi-Gaussian distribution, this becomes

$$\mathrm{RQI}^{*2} = \mathrm{RQI}_1^{*2}.x_1 + \mathrm{RQI}_2^{*2}.(1-x_1)\,. \tag{23}$$

By defining

$$\alpha = \mathrm{RQI}_1^*/\mathrm{RQI}_2^*\ ;\ \text{where}\ \alpha > 1\,, \tag{24}$$

we find that

$$\mathrm{RQI}_1^* = \alpha\ \mathrm{RQI}^*/\sqrt{1+(\alpha^2-1)x_1}. \tag{25}$$

Finally, Eq. (23) may be combined with Eq. (6) to give:

$$J^{*2}(S_w^*) = J^{*2}_1(S_w^*).x_1 + J^{*2}_2.(1-x_1)\,. \tag{26}$$

Eq. (26) enables El-Khatib (1995) J^*-function to support the modeling of bimodal rocks.

Multi-Gaussian and multimodal distributions are different but related concepts. While, the multi-Gaussian decomposition should be applied to any pore-throat-radius distribution which cannot be fitted by a single Gaussian distribution (see **Figure 2a**), a multimodal distribution requires at least two modes (or local maximum values), as shown in **Figure 2b**. To be able to predict, based on the corresponding parameters, which multi-Gaussian distribution will also be multimodal is not trivial. We combine Ashman et al. (1994) and Wang et al. (2009) approaches to propose the following bimodality index:

$$BI = \sqrt{2}\ \frac{\ln(r_{mode\,1}/r_{mode\,2})}{\sqrt{\sigma_1^2+\sigma_2^2}}\ \sqrt{x_1(1-x_1)}\quad , \tag{27}$$

Values of $BI \geq 0.75$ are considered good indicators of bimodality, while values of $BI \leq 0.25$ may be an indication that a single Gaussian distribution may be more appropriate (see Figure 2a and Figure 2b).

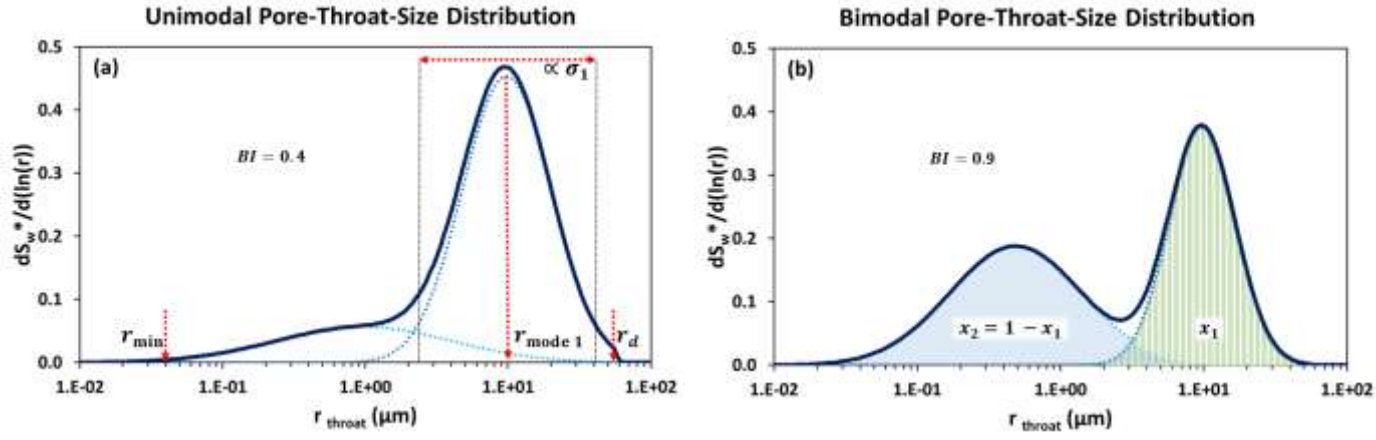

Figure 2 – (a) Typical bi-Gaussian, unimodal pore-throat-radius distribution with BI = 0.4 and (b) typical bimodal distribution with BI = 0.9. The pore-throat-radius PDF are plotted as continuous lines while individual Gaussian components are plotted as dotted lines. Bi-Gaussian decomposition parameters are also shown: the volumetric fraction x_1, the logarithmic pore-throat-radius mode $r_{mode\,1}$, the logarithmic standard deviation σ_1, the maximum pore-throat-radius r_d and the minimum pore-throat-radius r_{min}.

We should also distinguish between two other concepts: the multi-Gaussian component of a pore-throat-size distribution and the pore-system of a rock. While the multi-Gaussian decomposition is a purely mathematical concept, the pore system is a geological and petrophysical concept. Pore systems are defined by other properties than only pore-throat-size distribution: the pore-body-size distribution; percolation

path and threshold; pore connectivity, pore shape and mineralogy. Such properties are determined by the rock genesis and diagenesis history. Therefore, one single Gaussian distribution may comprise more than one pore system. On the other hand, a single pore system is frequently characterized by a single Gaussian pore-throat-size distribution, but it may eventually require a multi-Gaussian decomposition.

For example, in vuggy carbonates, we may differentiate between the rock matrix, isolated vugs and interconnected vugs. Isolated vugs are only connected through the matrix narrow pore throats while interconnected vugs are directly connected to each other. Isolated vugs and interconnected vugs will show different fluid-storage and transport behavior. Isolated vugs may be a result of the carbonate genesis, of selective matrix-mineral chemical transformation or selective matrix-mineral dissolution. Interconnected vugs may be the result of intense carbonate dissolution. In a typical vuggy carbonate rock with a bi-Gaussian pore-throat-size distribution, matrix and isolated vugs may correspond to the second Gaussian component, while the interconnected vugs may correspond to the first Gaussian component. Such concepts may be relevant for the dynamic characterization and simulation of complex carbonate reservoirs.

Universal J^{**}-Function

We start with the El-Khatib J^{*}-function Eq. (6) and the new RQI^{*} index Eq. (2), repeated below for clarity:

$$\mathrm{RQI}^{*} = \sqrt{k\tau_h/\phi_e} = \sqrt{\langle r_{\mathrm{throat}}^2 \rangle/8} \tag{2}$$

and

$$J^{*}(S_w^{*}) = \frac{P_c}{\gamma \cos(\theta)} \sqrt{\frac{k\tau_h}{\phi_e}} = \frac{2}{r_{\mathrm{throat}}} \sqrt{\frac{k\tau_h}{\phi_e}} = \frac{2\mathrm{RQI}^{*}}{r_{\mathrm{throat}}}. \tag{6}$$

Based on Eq. (11), we then propose a universal J^{**}-function for each Gaussian mode:

$$J^{**}(S_w^{*}) = \left(\frac{r_{\mathrm{mode}}}{r_{\mathrm{throat}}}\right)^{\frac{1}{\sqrt{2}\,\sigma}} = \left(\frac{r_{\mathrm{mode}}}{r_{\mathrm{throat}}} \frac{2\mathrm{RQI}^{*}}{2\mathrm{RQI}^{*}}\right)^{\frac{1}{\sqrt{2}\,\sigma}} = \left(\frac{r_{\mathrm{mode}}}{2\mathrm{RQI}^{*}} J^{*}(S_w^{*})\right)^{\frac{1}{\sqrt{2}\,\sigma}}. \tag{28}$$

Equation (11) then becomes our single-Gaussian, non-truncated, universal J^{**}-function formulation:

$$S_w^{*} = \frac{1}{2}\,\mathrm{erfc}(\ln(J^{**}))\,. \tag{29}$$

Considering the truncated S_w^{*} Eq. (13), then Eq. (29) becomes:

$$S_w^{*} = \frac{\mathrm{erfc}(\ln(J^{**})) - \mathrm{erfc}(\ln(J_{\mathrm{max}}^{**}))}{\mathrm{erfc}(\ln(J_d^{**})) - \mathrm{erfc}(\ln(J_{\mathrm{max}}^{**}))}\,, \tag{30}$$

Eqs. (15), (14) and (30) may be combined and generalized, considering a multi-Gaussian decomposition of pore-throat-size distribution, to get:

$$S_w^{**} = \frac{1}{2^n}\left\{\prod_{j=1}^{n}\left[\operatorname{erfc}\left(\ln\left(J_{d\,j}^{**}\right)\right) - \operatorname{erfc}\left(\ln\left(J_{max\,j}^{**}\right)\right)\right]\right\} \times \left\{S_w^{*} + \sum\nolimits_{i=1}^{n}\left[\frac{x_i \operatorname{erfc}\left(\ln\left(J_{max\,i}^{**}\right)\right)}{\operatorname{erfc}\left(\ln\left(J_{d\,i}^{**}\right)\right) - \operatorname{erfc}\left(\ln\left(J_{max\,i}^{**}\right)\right)}\right]\right\}, \tag{31}$$

and

$$\operatorname{erfc}\left(\ln\left(J_{mG}^{**}\right)\right) = \frac{1}{2^{(n-1)}}\left\{\prod_{j=1}^{n}\left[\operatorname{erfc}\left(\ln\left(J_{d\,j}^{**}\right)\right) - \operatorname{erfc}\left(\ln\left(J_{max\,j}^{**}\right)\right)\right]\right\} \times \left\{\sum\nolimits_{i=1}^{n}\left[\frac{x_i \operatorname{erfc}\left(\ln\left(J_{i}^{**}\right)\right)}{\operatorname{erfc}\left(\ln\left(J_{d\,i}^{**}\right)\right) - \operatorname{erfc}\left(\ln\left(J_{max\,i}^{**}\right)\right)}\right]\right\}, \tag{32}$$

By combining Eqs. (31) and (32) we get the multi-Gaussian J_{mG}^{**}-function concise form:

$$S_w^{**} = \frac{1}{2}\operatorname{erfc}\left(\ln\left(J_{mG}^{**}\right)\right). \tag{33}$$

Eq. (33) is compact. No parameters are required other than the implicit multi-Gaussian parameters stored in J_{mG}^{**}. No implicit assumptions are made except that the rock is single-wetted and under drainage process. It does not require any curve averaging. Therefore, Eq. (33) is also algebraically universal.

Provided the multi-Gaussian decomposition suitably fits the pore-throat-size distribution, applying Eqs. (31), (32) and (33) over any drainage capillary pressure data results in a plot superimposing a segment of the generic curve $y = \frac{1}{2}\operatorname{erfc}\left(\ln(x)\right)$, where $x > 0$.

In the case of bi-Gaussian rocks, Eqs. (31) and (32) are simplified:

$$\begin{aligned} S_w^{**} = \frac{1}{4}\Big\{ & S_w^{*}\left(\operatorname{erfc}\left(\ln\left(J_{d\,1}^{**}\right)\right) - \operatorname{erfc}\left(\ln\left(J_{max\,1}^{**}\right)\right)\right)\left(\operatorname{erfc}\left(\ln\left(J_{d\,2}^{**}\right)\right) - \operatorname{erfc}\left(\ln\left(J_{max\,2}^{**}\right)\right)\right) \\ & + x_1 \operatorname{erfc}\left(\ln\left(J_{max\,1}^{**}\right)\right)\left(\operatorname{erfc}\left(\ln\left(J_{d\,2}^{**}\right)\right) - \operatorname{erfc}\left(\ln\left(J_{max\,2}^{**}\right)\right)\right) \\ & + (1 - x_1)\operatorname{erfc}\left(\ln\left(J_{max\,2}^{**}\right)\right)\left(\operatorname{erfc}\left(\ln\left(J_{d\,1}^{**}\right)\right) - \operatorname{erfc}\left(\ln\left(J_{max\,1}^{**}\right)\right)\right)\Big\}, \end{aligned} \tag{34}$$

and

$$\begin{aligned} \operatorname{erfc}\left(\ln\left(J_{mG}^{**}\right)\right) = \frac{1}{2}\Big\{ & x_1 \operatorname{erfc}\left(\ln\left(J_{1}^{**}\right)\right)\left(\operatorname{erfc}\left(\ln\left(J_{d\,2}^{**}\right)\right) - \operatorname{erfc}\left(\ln\left(J_{max\,2}^{**}\right)\right)\right) \\ & + (1 - x_1)\operatorname{erfc}\left(\ln\left(J_{2}^{**}\right)\right)\left(\operatorname{erfc}\left(\ln\left(J_{d\,1}^{**}\right)\right) - \operatorname{erfc}\left(\ln\left(J_{max\,1}^{**}\right)\right)\right)\Big\}, \end{aligned} \tag{35}$$

Averaging the J_{mG}^{**} curves for different samples is not required. The fit to the generic curve (Eq. (33)) is a measurement of how good is the sample's multi-Gaussian decomposition. Using the universal J^{**} function for this checking purpose allows the more practical and equally universal combination of Eqs. (3), (7), (12), (15) and (14). These equations easily and precisely allow reconstructing any single-wetting drainage capillary pressure curve from its multi-Gaussian decomposition parameters.

Data Setup

We apply the truncated multi-Gaussian decomposition to the Worldwide Rock Catalog (WWRC) data and analyze several possible correlations within the results. This catalog is the result of a joint-industry project. It comprises carbonate and clastic samples from around the world. We selected 45 out of 49 carbonate rock samples for our present study. We also took 105 clastic samples from the WWRC to further validate the proposed multi-Gaussian decomposition method. The samples are categorized according to geological and petrophysical criteria (Dunham, Lucia and Archie's classifications), allowing the analysis of rock-property correlations for specific facies. We use data from routine core analysis, steady state mercury-injection capillary pressure (MICP), and SCAL (saturation-end points from water-gas-drainage capillary pressure and oil-water-imbibition relative permeability). Gas absolute permeability is corrected according to Klinkenberg (1941). With a few exceptions, the different experiments were run on the same core plugs, increasing the likelihood of correlation between different derived properties.

MICP experiments are relatively cheap and precise. They have progressively become more important in carbonate reservoir characterization. Therefore, we believe there is a large potential for future application of our proposed methods to other carbonate fields.

We propose the following workflow:

- Remove any eventual residual Hg dead volume and closure effects;
- Calculate the pore-throat equivalent radius for each capillary pressure step, using Eq. (3);
- Determine maximal pore-throat radius r_d corresponding to the capillary entry pressure P_d, where mercury saturation starts to increase;
- Determine minimum pore-throat radius $r_{\min}$ corresponding to the maximum mercury injection pressure where mercury saturation ceases to increase;
- Calculate the normalized air-saturation S_{w}^{*} and the incremental $\Delta S_{\mathrm{w}}^{*}$ for each pressure step;
- Calculate the MICP average pore-throat squared radius $\langle r_{\mathrm{throat}}^{2} \rangle$;
- Calculate hydraulic tortuosity τ_h;
- Determine R_{35} at $S_{\mathrm{Hg}} = 35\%$;
- Calculate the rock-typing indexes: RQI, FZI, Winland R35 and RQI*;
- Calculate the increment of logarithmic pore-throat radius $\Delta \ln(r_{\mathrm{throat}})$ for each pressure step;
- Plot the PDF of $\ln(r_{\mathrm{throat}}) = \Delta S_{\mathrm{w}}^{*} / \Delta \ln(r_{\mathrm{throat}})$;
- From the PDF plot obtain first guesses for $r_{mode\,1}$, $r_{mode\,2}$, σ_1, σ_2 and x_1;
- Calculate the first guess of the bi-Gaussian normalized wetting-saturation as a function of pore-throat-radius from Eq. (16);
- Use multivariate regression analysis (or similar curve fitting optimizing method) to minimize the minimum mean square error of both the PDF of $\ln(r_{\mathrm{throat}})$ (direct method) and S_{w}^{*} (inverse method). To ensure the stability of the optimization, we set the constraint: $r_{\mathrm{mode}\,1} / r_{\mathrm{mode}\,2} \geq 2$;
- For each set of bi-Gaussian decomposition parameters, calculate the multi-Gaussian universal $J_{mG}^{**} \times S_{w\,mG}^{**}$ curve, from Eqs. (31) and (32). Compare the results with the theoretical curve described by Eq. (33);
- For each set of parameters, calculate the adjusted average pore-throat squared radius $\langle r_{\mathrm{throat}}^{2} \rangle$ by using Eqs. (20) and (21). Compare the adjusted $\langle r_{\mathrm{throat}}^{2} \rangle$ to the MICP $\langle r_{\mathrm{throat}}^{2} \rangle$ values;
- Validate $\langle r_{\mathrm{throat}}^{2} \rangle$ and the universal J_{mG}^{**}-function results. Then compare both sets of bi-Gaussian decomposition parameters and corresponding results to solve any eventual fitting issues;
- Calculate the corresponding Ashman / Wang bimodal index.

A good characterization of the larger pore-throat-size range may require a low-pressure range MICP experiment and accurate dead volume and closure corrections. We also recommend avoiding the use of capillary pressure fitting models as they may misrepresent the actual low-pressure MICP data. Modern MICP experiments already provide very good pore-throat-distribution characterization in the low-pressure range. MICP experiments present no wettability issues, are consistent with gas corrected permeability, cover a large pressure range and usually result in very low residual-air saturation.

Results of Truncated Multi-Gaussian Pore-Throat-Size Decomposition

All MICP pore-throat-size distributions were fit by bi-Gaussian decomposition with five independent parameters: $r_{mode\,1}$ and $r_{mode\,2}$; σ_1 and σ_2; and x_1. Whenever a single Gaussian was appropriate, it was automatically selected.

Generally, both direct and inverse approaches resulted in good fitting quality. From 155 carbonate and clastic samples, 135 (87%) resulted in similar sets of decomposition parameters after direct and inverse automatic fitting processes. Only 15 samples (9.7%) required manual intervention to adjust parameters and select the best solution. One clastic and four carbonate samples would have required a tri-Gaussian decomposition. Therefore, we excluded those five samples from the dataset. Considering the truncation of the pore-throat-size distribution was a key aspect to improve the stability of the method and the fitting quality.

We present three carbonate examples of bi-Gaussian decomposition, extracted from the results.

Figure 3a presents a bi-Gaussian, unimodal pore-throat-size distribution for Sample 1 with an excellent fit to the MICP data. **Figure 3b** confirms the fitting quality through the match between the theoretical and actual bi-Gaussian J^{**}-functions, across the entire normalized saturation range.

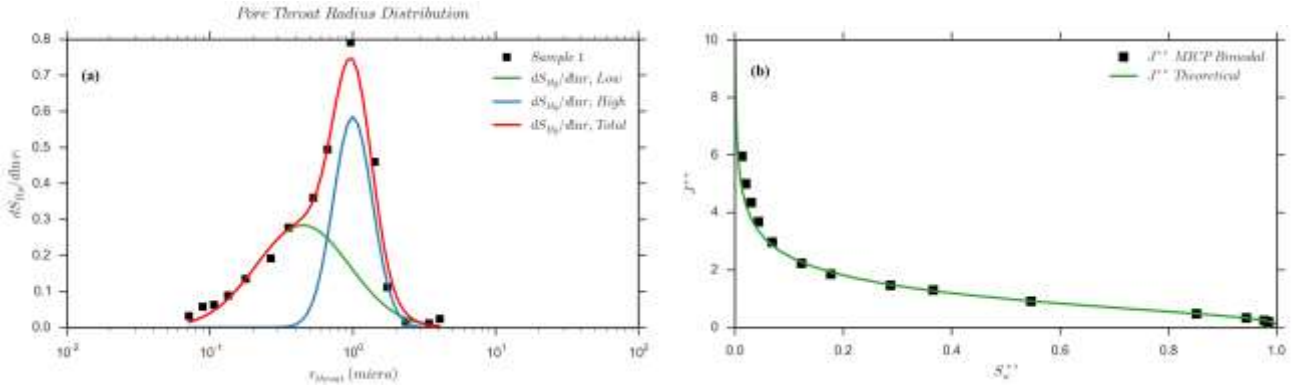

Figure 3 – (a) Bi-Gaussian decomposition of unimodal carbonate Sample 1 and (b) the corresponding J^{**} validation.
In (a), black dots correspond to the actual MICP data; the blue curve corresponds to the first Gaussian component; the green curve corresponds to the second Gaussian component; and the red curve corresponds to the resulting bi-Gaussian composition.
In (b), the green curve corresponds to the theoretical J^{**} curve and the black dots correspond to the bi-Gaussian J^{**} obtained from the MICP data.

Figure 4a presents a multimodal distribution for Sample 2. The bi-Gaussian fit is not so good; a tri-Gaussian decomposition may be more appropriate. Nevertheless, the bi-Gaussian decomposition met the universal J_{mG}^{**}-function criteria as shown in **Figure 4b**. Sample 2 is a good example where considering the truncation parameters is very important for a proper fit. In the WWRC, the maximum MICP pressure is 2,000 psi, therefore $r_{\min}$ is likely limited by the experiment. Consequently, the resulting Gaussian distribution may be extrapolated to consider a smaller $r_{\min}$ if a proper correlation is available. Conversely, r_{d} is likely limited by nature, as the distribution shows, after closure correction, a first injection step with

a very small saturation change. **Figure 4b** also shows the normalized saturation limits corresponding to the truncation of the distribution.

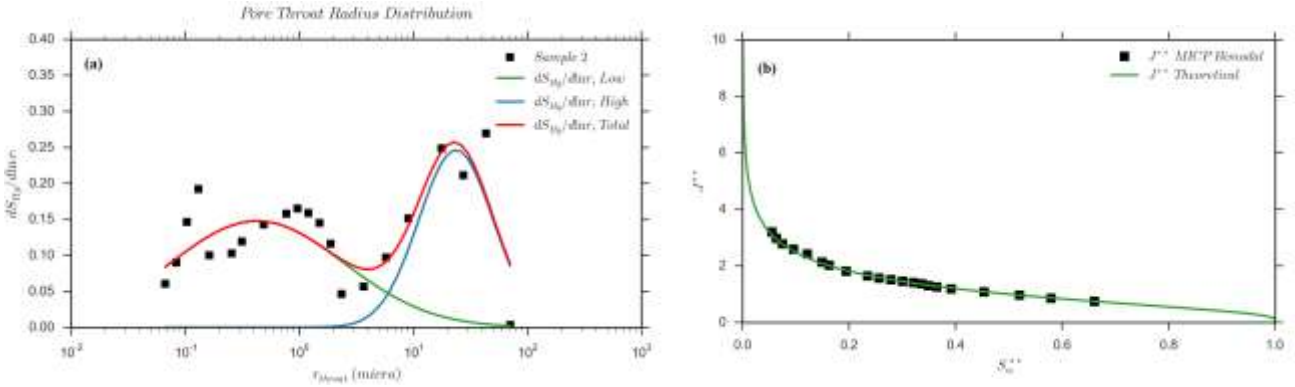

*Figure 4 - (a) Bi-Gaussian decomposition of multimodal carbonate Sample 2 and (b) the corresponding J** validation*

Figure 6a presents a bi-Gaussian, bimodal distribution for Sample 3 with a good fit to the MICP data. **Figure 6b** confirms the fitting quality through a good match between the theoretical and actual bi-Gaussian J**-functions.

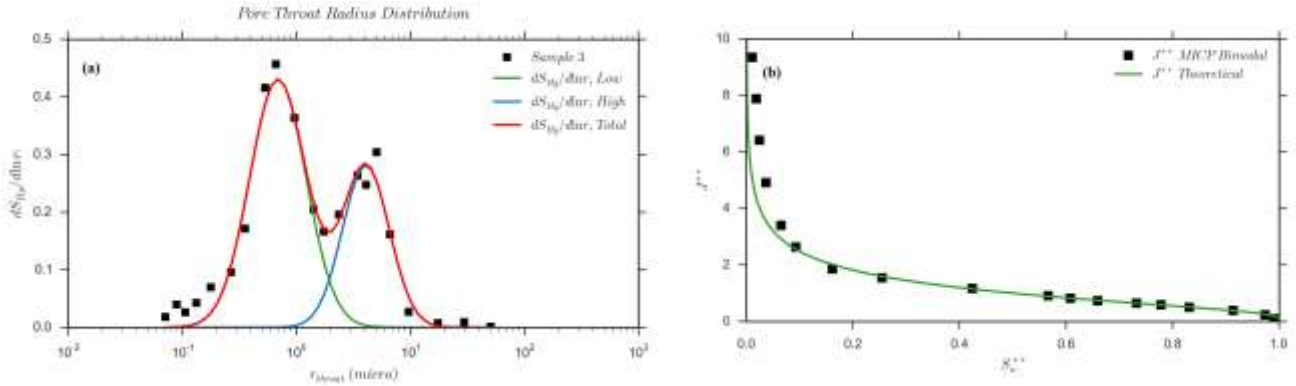

*Figure 6 – (a) Bi-Gaussian decomposition of bimodal carbonate Sample 3 and (b) the corresponding J** validation*

Figure 5 presents a comparison between Leverett J-function, El-Khatib J^*-function and the proposed bi-Gaussian J^{**}-function, for Sample 1 (**Figure 5a**) and Sample 2 (**Figure 5b**). J and J^* curves for Sample 2 show a stronger inflection due to its bimodality when compared to Sample 1 curves. Sample 2 also shows a larger separation between J and J^* curves, because its hydraulic tortuosity $\tau_h = 47$ is much larger when compared to Sample 1 tortuosity $\tau_h = 3.5$. The J^* curves are different from each other because of their differences in bimodality and pore-size sorting.

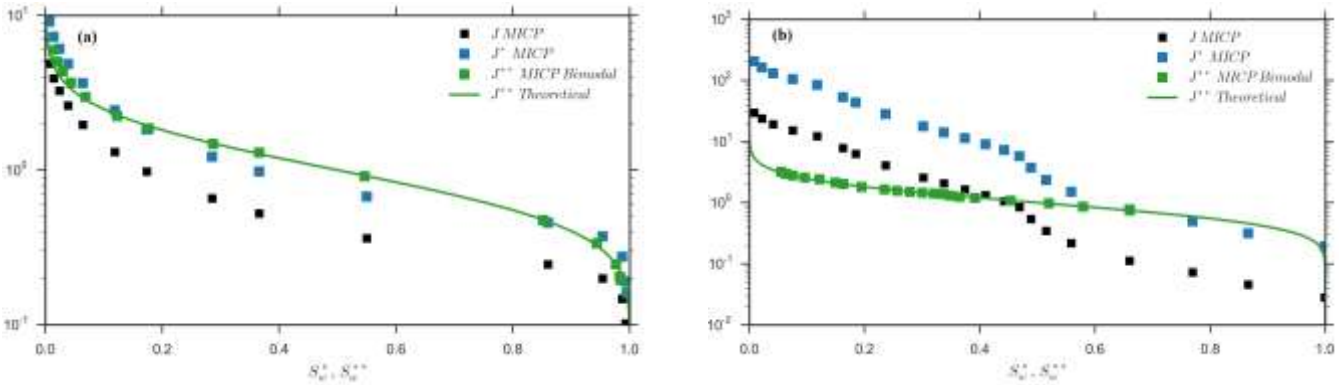

Figure 5 – Comparison between Leverett J-function, El-Khatib J-function and J**-function for (a) Sample 1 and (b) Sample 2*

Nevertheless, the actual bi-Gaussian J^{**} are the same for both samples, except for the truncated part of the distribution, which is stronger in the case of Sample 2, showing the universal aspect of J^{**}.

Figure 7 summarizes the bi-Gaussian overall fitting quality by comparing the adjusted average pore-throat squared radius $\langle r^2_{\text{throat}} \rangle$ to the MICP $\langle r^2_{\text{throat}} \rangle$ values, for both clastics (**Figure 7a**) and carbonates (**Figure 7b**) WWRC samples. Both results show an excellent linear correlation.

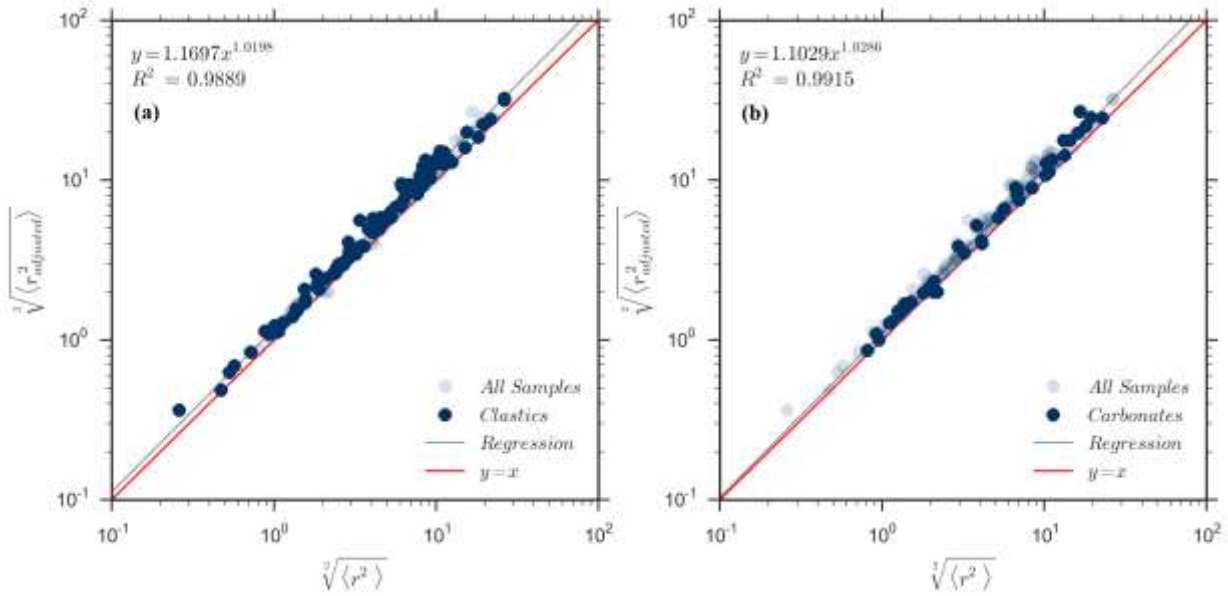

Figure 7 – Comparison between the adjusted average pore-throat squared radius $\langle r^2_{throat} \rangle$ and the MICP $\langle r^2_{throat} \rangle$ values for both (a) clastic and (b) carbonate samples.

Figure 8 summarizes the degree of bimodality for both clastics (**Figure 8a**) and carbonates (**Figure 8b**). The results are based on the Ashman Wang's modified index BI defined by Eq. (27).

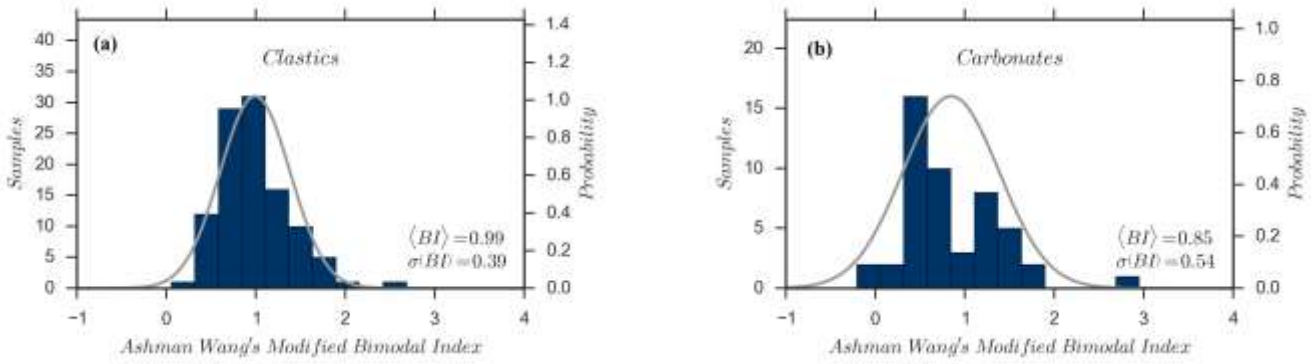

Figure 8 – Bimodality of the WWRC samples for both (a) clastics and (b) carbonates, based on the Ashman Wang's modified index BI.

Among the 45 selected carbonate samples, 4 samples may be well fitted by a single Gaussian distribution, 21 bi-Gaussian samples are unimodal, and the remaining 20 samples are both bi-Gaussian and bimodal. Interestingly, among the 105 selected clastic samples, only one may be well fitted by a single Gaussian distribution, 24 bi-Gaussian samples are unimodal, and the remaining 80 are bi-Gaussian and bimodal.

Therefore, not only the WWRC carbonate rocks show a large multimodality variability, but also the WWRC clastic rocks present significant multimodal characteristics.

Figure 9 presents the volumetric fraction x_1 of the first Gaussian component for both WWRC carbonates (**Figure 9a**) and limestones (**Figure 9b**). Clastic and dolostones samples (not shown) also presented similar mean and standard deviation values for x_1.

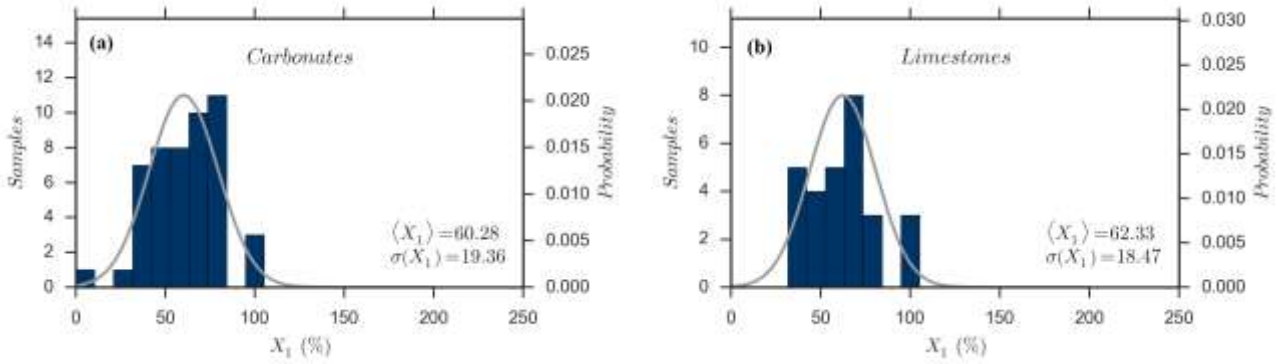

*Figure 9 – Volumetric fraction x_1 of the first Gaussian component for both WWRC carbonates (**a**) and limestones (**b**) samples.*

Similar to Xu and Torres-Verdín (2013), we also found interesting correlations between bi-Gaussian decomposition parameters and rock properties.

Figure 10a presents the correlation between the larger pore-throat size r_d and the first Gaussian mode $r_{\text{mode 1}}$ for the WWRC carbonates samples.

Figure 10b presents the correlation between r_d and the average pore-throat squared radius $\sqrt{\langle r_{\text{throat}}^2 \rangle}$.

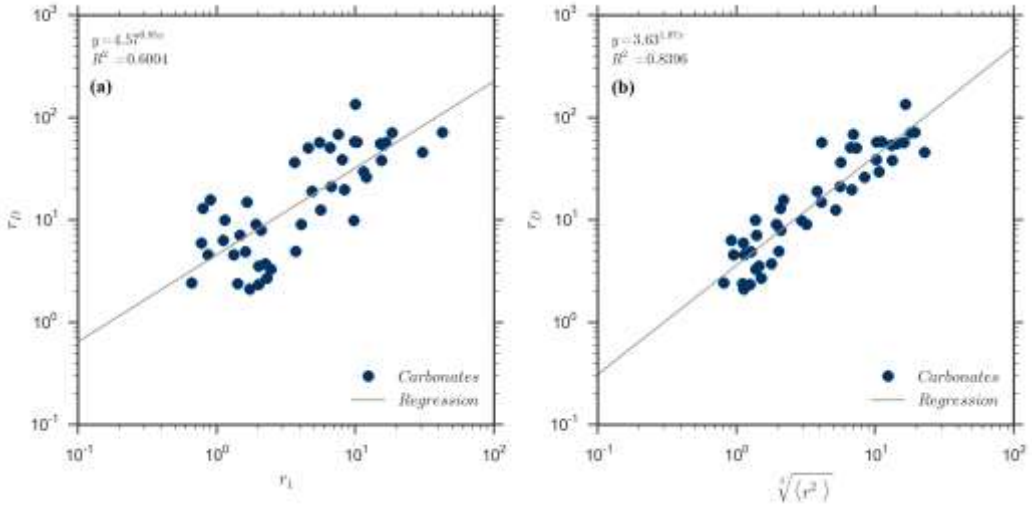

*Figure 10 – Larger pore-throat size r_d correlation with (**a**) the first Gaussian mode $r_{mode\ 1}$ and (**b**) the average pore-throat squared radius $\sqrt{\langle r_{throat}^2 \rangle}$, for the WWRC carbonates samples.*

The later correlation is unexpectedly strong, particularly considering that the WWRC samples do not belong to the same field but come from all over the world. A possible explanation is that $\sqrt{\langle r_{\text{throat}}^2 \rangle}$ accounts for both $r_{mode\ 1}$ and σ_1.

The above correlations confirms the importance of the truncation (r_d and corresponding P_d) to dynamic reservoir characterization, as presented by Thomeer (1960) and Clerke et al. (2008).

Figure 11 presents the correlation between the irreducible water saturation (from gas-water capillary pressure) S_{wirr} and the second Gaussian mode $r_{\mathrm{mode}\,2}$, for both carbonate (**Figure 11a**) and limestone samples (**Figure 11c**). The correlations are weak, but we need to consider that the WWRC samples come from all over the world. Data from a single field are expected to have better correlation coefficients.

Equation (11) suggests that the irreducible water saturation may be more closely correlated with the term $\ln(r_{\mathrm{mode}\,2})/(\sqrt{2}\sigma_2)$, which consider the standard deviation of the second Gaussian component σ_2 in addition to r_2. **Figure 11** also presents the correlation between the irreducible water saturation (from gas-water capillary pressure) S_{wirr} and such term for both carbonates (**Figure 11b**) and limestones (**Figure 11d**). Although the correlation coefficient is significantly improved, this result is heavily influenced by a few points with high irreducible water saturation. To confirm a good correlation we should have more points. Nevertheless, this is an example of the potential of correlation between the multi-Gaussian parameters and rock properties. Data from a specific field may show a stronger correlation.

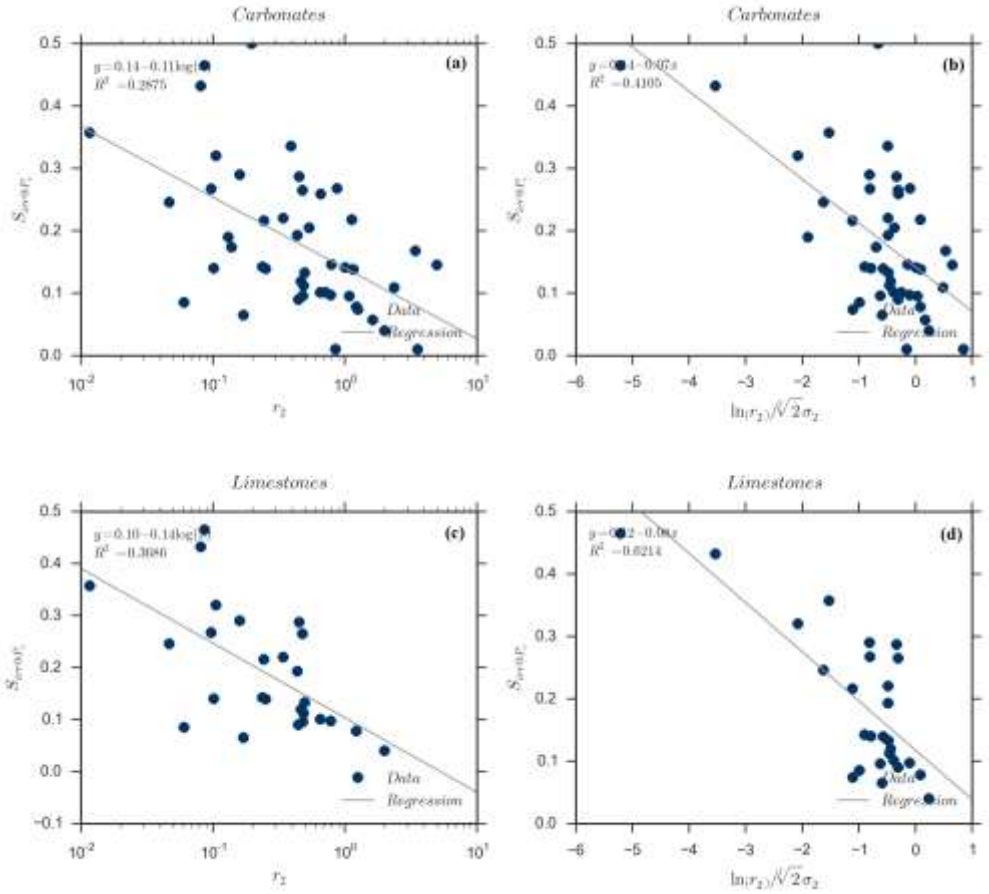

*Figure 11 – Correlation of irreducible water saturation (from gas-water capillary pressure) S_{wirr} with the second Gaussian mode r_2 for both (**a**) WWRC carbonates (**c**) and limestones. Improved correlation of irreducible water saturation (from gas-water capillary pressure) S_{wirr} with the term $ln(r_{mode\,2})/(\sqrt{2}\sigma_2)$ for the second Gaussian component, for both (**b**) carbonates (**d**) and limestones.*

From these results, our truncated multi-Gaussian pore-throat-size decomposition may be a significant improvement compared with the Thomeer (1960) multimodal hyperbola method.

Our method properly considers the experimental or natural limits of the data – the maximum r_d and the minimum pore-throat-radii r_{min}, which may be relevant to the fitting quality as shown in Figure 4. Thomeer method only considers the entry pressure P_d, which corresponds to r_d.

Thomeer method uses P_d as adjusting parameter for each modal while in our method, we may choose to preserve the observed P_d (or r_d) instead of using it as a fitting parameter.

The multi-Gaussian decomposition parameters: $r_{mode\,i}$; σ_i; $r_{d\,i}$; $r_{\min i}$ and x_i have a clear statistical meaning. Such decomposition parameters, when compared to Thomeer's parameters, may be easier to upscale and correlate to other core and well log measurements, e.g. NMR. The statistical nature of these parameters may also help to improve the upscaling of other rock properties. These new and meaningful parameters, and their combination, may explicit new correlations with rock properties, as shown earlier in Figure 10 and Figure 11. Such parameters, may also be used together with RQI* to enhance the dynamic rock-typing process for reservoir simulation of IOR / EOR in complex carbonate rocks.

Pore-Throat-Radius Distribution and Bimodality in Reservoir Simulation

To our knowledge, commercial reservoir simulation software does not directly support truncated multi-Gaussian pore-throat-radius distributions, the proposed J^{**}-function, hydraulic tortuosity, nor the El-Khatib J^{*}-function.

To date, we have not implemented a suitable workaround to simulate J^{**}-function in commercial simulation software because of the non-linear nature of J^{**} with respect to the pore-throat-radius standard deviation $\sigma(r_{\text{throat}})$. Nevertheless, for fixed $\sigma(r_{\text{throat}})$ for each rock type and corresponding reservoir saturation region, we may then use Eq. (28) and the workaround proposed by Ferreira et al. (2015), implemented by coherently changing both the permeability and the transmissibility multipliers, in order to allow the Leverett J-function, available in the simulator, to capture the El-Khatib J^{*}-function, while preserving the model transmissibility.

We also replace RQI with RQI* to map the corresponding rock types to the simulator rock regions. The following equations summarize the simulation workaround (for each pore-system):

$$\text{RQI}^{*} = \text{RQI}\,\sqrt{\tau_h}\,, \tag{36}$$

$$J^{*}(S_w^{*}) = J(S_w^{*})\,\sqrt{\tau_h}\,, \tag{37}$$

$$k^{*} = k\,\tau_h\,, \tag{38}$$

$$T_M^{*} \cong {T_M}/{\tau_h}\,, \tag{39}$$

where in fact the modified transmissibility multiplier T_M^{*} calculation depends on the specific transmissibility calculation algorithm used by the simulator software. For more details, see Ferreira et al. (2015).

In addition to such a workaround, we consider a dual/triple porosity approach to separately simulate the capillary behavior of different pore-systems, e.g. matrix (with or without isolated vugs) and connected vugs. We assume that each of such pore systems directly corresponds to a Gaussian component. For each porosity system, we then use the simulation workaround above to include the correlated concepts of J^{*}-function, hydraulic tortuosity and average squared pore-throat radius.

In a vuggy-rock dual-porosity simulation, to properly consider the interactions between the porosity system corresponding to the matrix (with or without isolated vugs) and the porosity system corresponding

to the connected vugs, we need to calculate the matrix-to-connected-vugs transmissibility / diffusivity coefficient σ_v, defined by Kazemi et al. (1976) as:

$$\sigma_v = 4\left(1/l_x^2 + 1/l_y^2 + 1/l_z^2\right), \tag{40}$$

where l_x, l_y and l_z are typical dimensions of the matrix blocks of material making up the matrix volume, and are thus not related to the simulation grid dimensions. Note that σ_v is completely unrelated to the σ used to denote the standard deviation of probability distributions. Equation (40) was derived for matrix-fracture systems. Nevertheless, we assume that this is also valid for the transport between the matrix and the system of connected vugs. A key difference in the use of dual porosity simulation in this case is that the matrix blocks may be several orders of magnitude smaller than the ones found in typical matrix-fracture systems, resulting in much larger σ_v values.

Finally, Gurpinar et. al (1999) introduced a method to obtain, for matrix rock surrounding non-connected vugs, composite capillary pressure and relative permeability curves for primary drainage, imbibition and secondary drainage.

Multimodality Variability Impact on Oil-in-Place and Reserves Estimates

The balance between the benefits and costs determines the value of a dynamic reservoir characterization process. Acquiring and analyzing data from cores, well logs, well tests and other surveys set the costs. The resulting decreased reservoir characterization uncertainties defines the benefits. A sensitivity analysis of the impact of the reservoir uncertainties over the field economics quantifies such benefits. In this paper, we have so far investigated the distribution of pore-throat radius within individual rock samples. In the reservoir, there will be many rock types, with corresponding spatial variability in the parameters that characterize the multimodal pore-throat-size distributions. The spatial variability of rock types may affect uncertainty in both absolute permeability and capillary effects. In a similar manner to Ferreira et al. (2015), we present a sensitivity study focused on the impact of variability of parameters describing the bimodal pore-throat radius distribution on capillary effects, i.e. capillary pressure and relative permeability curves. We do not consider any impact on the absolute permeability. We consider two main impacts of bimodality variability on dynamic characterization: the fluid-saturation distribution in the transition zone, influenced by capillary pressure curves; and the decrease of displacement-fluid sweep efficiency due to fingering and channeling, mainly influenced by relative permeability curves, saturation end-points, rock heterogeneity and fluid-mobility ratio (M).

First, let us consider a bimodal system with characteristic parameters: $r_{mode\,1}$; $r_{mode\,2}$; σ_1; σ_2 and x_1. Ferreira et al. (2015) presented a sensitivity study on the impact of hydraulic tortuosity variability on capillary effects. According to Eq. (1), such sensitivity results are equivalent to the sensitivity on $\langle r_{\mathrm{throat}}^2 \rangle$ variability. According to Eq. (20), $\langle r_{\mathrm{throat}}^2 \rangle$ is defined by r_{mode} and σ. Therefore, most of the impact of the variability of pore-throat-size mode r_{mode} and standard deviation $\sigma\left(ln(r_{\mathrm{throat}})\right)$ has already been covered by Ferreira et al (2015). Consequently, in this study we focus on the impact of x_1, the volumetric fraction of the first pore system, on capillary effects, oil-in-place (OOIP) and total reserves, which corresponds to the ultimate cumulative reservoir production (N_p).

We use the same synthetic simulation model as Ferreira et al. (2015), converted to a dual-porosity system. Eqs. (24) and (25) are used to calculate RQI_1^* and RQI_2^* as a function of RQI^* and x_1.

We maintain the same mean value of hydraulic tortuosity $\langle \tau_h \rangle = 40$ fixed for both porosity systems, with standard deviation $\sigma(\tau_h) = 0$. In so doing, the sensitivity results of the impact of the volumetric fraction x_1 of the first Gaussian component supplement the results of Ferreira et al. (2015).

For each porosity system and rock type, we use Eqs. (13) and (6) to obtain El-Khatib J^* curves from the corresponding truncated single Gaussian pore-throat-size distribution and the mean tortuosity value. For each dynamic-reservoir-rock type (DRRT) or saturation region, we consider a fixed $\sigma(r_{\text{throat}})$. With this approach, we create an equivalent Leverett J-function curve for each rock type (see Eq. (37)), consistent with the corresponding ranges of RQI and RQI*. For simplicity, the reservoir rock is moderately water-wet, with no fractures or isolated vugs.

To calculate the correct transmissibility / diffusivity coefficient σ_v between the matrix and the connected-vugs, we use Eq. (40).

For the sensitivity study, we also considered three different synthetic mobility-ratio cases: light, average and heavy oil, where oil densities and viscosities were set according to typical industry ranges, as shown in Table 1 . Under water injection, such cases approximately correspond to mobility ratios of 1, 10 and 100.

Table 1 - Fluid Properties for the Sensitivity Study

Fluid Properties	API	Psat (psia)	Boi @ 5000 psia	μoi (cP)	Rsi (scf/stb)
Light Oil	35	2500	1.275	0.66	568
Average Oil	20	1500	1.103	5.2	183
Heavy Oil	15	1000	1.088	71.25	92

Table 2 shows the main parameters and strategies to distribute the synthetic reservoir properties throughout the simulation model grid. The property distribution workflow, including variogram parameters, follows Ferreira et al. (2015).

Table 2 - Sensitivity Study Property Distribution

Property	Type	Mean	Std. Dev.
Effective Porosity ϕ_e	*Normal*	20%	3.5%
RQI	*Lognormal*	0.6 μm	0.3 μm
Absolute Permeability ($k_x = k_y$)	$k_{x,y} = RQI^2 . \phi_e$	96 mD	96 mD
k_z/k_x	*Normal*	0.3	0.1
Absolute Permeability (k_z)	$k_z = (k_z/k_x) . k_x$	29 mD	33 mD
Hydraulic Tortuosity ($\tau_x = \tau_y$)	*Lognormal*	40	0
Hydraulic Tortuosity (τ_z)	$\tau_z = \tau_x . k_x/k_z$	170	687

Table 3 shows the additional parameters and strategies to convert the simulation model prepared by Ferreira et al. (2015) to a dual-porosity model.

Table 3- Sensitivity Study Dual-Porosity Property Distribution

Property	**Type**	**Mean**	**Std. Dev.**
First Gaussian volumetric fraction (x_1)	*Normal*	{40-60-80%}	{0, 20%}
Ratio $\alpha = \mathrm{RQI}_1^*/\mathrm{RQI}_2^*$	*Estimated*	20	-
RQI_1^*(connected vugs)	Eq. (26)	5.7 μm	2.7 μm
RQI_2^*(matrix)	Eq. (25)	.29 μm	0.14 μm
Matrix block size $(l_x = l_y = l_z)$	*Estimated*	100 μm	-
Matrix-to-connected-vugs coefficient σ_v	Eq. (40)	1.1e08 ft^{-2}	-
Log. pore-throat size standard deviation:	*Function of DRRT*	$\sigma(\ln(r_{\mathrm{throat}}))$	
DRRT 1	$\mathrm{RQI}^* \leq 1.3$	3	-
DRRT 2	$1.3 \leq \mathrm{RQI}^* \leq 2.5$	2.5	-
DRRT 3	$2.5 \leq \mathrm{RQI}^* \leq 4.9$	2	-
DRRT 4	$4.9 \leq \mathrm{RQI}^* \leq 9.6$	1.5	-
DRRT 5	$\mathrm{RQI}^* > 9.6$	1	-

Our base case corresponds to a homogeneous first Gaussian volumetric fraction $\langle x_1 \rangle = 60\%$. We then create multiple stochastic realizations to investigate the sensitivity to heterogeneity in first Gaussian volumetric fraction with $\langle x_1 \rangle = 60\%$ and $\sigma(x_1) = 20\%$.

Finally, if the variability of the first Gaussian volume fraction $\sigma(x_1)$ is high, the core sampling for the capillary pressure and relative permeability experiments may unintentionally miss the mean value of $\langle x_1 \rangle$. Therefore, if no corrections are made, such experimental results are defined by the actual volume fraction x_1 of the samples, and do not represent the average capillary behavior for the corresponding rock types. To assess the corresponding impact, we run two additional light-oil $(M \leq 1)$ sensitivity base cases, with $\langle x_1 \rangle$ at 40% and 80%, while keeping the standard deviation $\sigma(x_1)$ equal to zero. We then compare these two cases with the light-oil case with $\langle x_1 \rangle = 60\%$ and $\sigma(x_1) = 0\%$.

Table 4 summarizes the results from this sensitivity study.

Table 4 – Bimodal Volume Fraction Variability Sensitivity Results

	$\sigma(x_1)$ Impacts			Missing $\langle x_1 \rangle$ in SCAL	
$\langle x_1 \rangle$	60%			40%→60%	60%←80%
$\sigma(x_1)$	0→20%			0	
M	M ≤ 1	M = 10	M = 100	M ≤ 1	M ≤ 1
ΔOOIP	-1.5%	-2.2%	-2.5%	22%	-16%
$\Delta \mathrm{Np}_{\mathrm{reservoir}}$	-3.8%	-3.4%	-3.2%	30%	-31%
$\Delta \mathrm{Np}_{\mathrm{well}}$	-3.5%	-3.6%	-5.1%	-	-

The impact of the variability of the Gaussian volume fraction $\sigma(x_1) = 20\%$ around its mean value $\langle x_1 \rangle = 60\%$ on oil-in-place and reserves is small, between 1.5 and 5.1%. Furthermore, the small changes of such impacts with the mobility ratio M suggest that the fingering effects are negligible. Therefore, all the impacts are assigned to the transition-zone effect.

The results were insensitive to different values of the matrix-to-connected-vugs coefficient σ_v. The likely reasons are the water-injection voidage-replacement fraction being equal to one, maintaining the reservoir pressure close to its initial value; the large ratio between the smaller and larger pore-throat-size modes; the prevalence of viscous forces over the capillary ones; the water-wet assumption and the no hysteresis assumption. A more comprehensive sensitivity study was out of the scope of this paper.

The fact that almost all production comes from the connected vugs helps to explain the lack of sensitivity to x_1. Since the two pore-throat-radius distributions are well separated, the only significant effect of varying x_1 is to vary the porosity of the two corresponding pore systems. Unlike the upscaling of absolute permeability and relative permeability, the upscaling of porosity is linear and leads to an upscaled porosity equal to the average porosity. For this reason, the oil-in-place and reserves are only significantly sensitive to the average value of x_1 and not its variability.

Conversely, Ferreira et al. (2015) found significant impacts of variability in the hydraulic tortuosity with the increasing mobility ratio M. The hydraulic tortuosity has a significant impact on the relative permeability via RQI* and corresponding rock types, which cannot be upscaled using average values (especially for higher mobility ratios). The heterogeneity in the relative permeability leads to increased heterogeneity in the fluid saturation, resulting in a decrease in sweep efficiency.

Table 4 also shows the significant impact on OOIP and N_p estimates when we unintentionally miss the mean value of the first Gaussian volume fraction $\langle x_1 \rangle$ during the SCAL sampling. In the transition zone, the water saturation in the first pore system is always smaller when compared to the water saturation in the second pore system. Therefore, when the SCAL Gaussian volume fraction ($\langle x_1 \rangle = 60\%$) is greater than the actual reservoir mean value ($\langle x_1 \rangle = 40\%$), the water saturation in oil-water-transition zone will be smaller in the reservoir simulation model than it actually is. OOIP is then severely overestimated by simulation, as well as the ultimate reserves. Conversely, when the SCAL Gaussian volume fraction ($\langle x_1 \rangle = 60\%$) is smaller than the actual reservoir mean value ($\langle x_1 \rangle = 80\%$), OOIP and N_p are drastically underestimated by simulation. Therefore, we recommend applying proper corrections while deriving dynamic reservoir properties from capillary pressure and relative permeability experiments, based on the J^* and RQI^* concepts. We may use Eq. (26) to correct the capillary pressure results from the sample Gaussian volume fraction to the reservoir mean value obtained from MICP or well log data. Likewise, we may use Eq. (23) to correct the relative permeability curves parameters and corresponding end-points.

The results of this paper shown in Table 4 supplement the results of Ferreira et al. (2015). Their results on the impacts of the hydraulic-tortuosity sensitivity on OOIP and N_p are summarized in Table 5.

Table 5 - Tortuosity Variability Sensitivity Results

	Transition-Zone Effect			Fingering Effect			Missing $\langle \tau_h \rangle$ in SCAL	
$\langle \tau_h \rangle$	40			40			10→40	40←100
$\sigma(\tau_h)$	0→40			0→40			0	
M	M ≤ 1	M = 10	M = 100	M ≤ 1	M = 10	M = 100	M ≤ 1	M ≤ 1
ΔOOIP	-8%	-9%	-10%	0	0	0	45%	-18%
$\Delta Np_{reservoir}$	-18%	-23%	-61%	-3%	-7%	-13%	202%	-33%
ΔNp_{well}	-19%	-24%	-69%	-6%	-13%	-27%	–	–

We may mitigate the effects on the transition zone (Table 4 and Table 5) by artificially reconciling SCAL corrections (from laboratory to reservoir conditions) with high-quality water-saturation well logs. However, we cannot mitigate the impact on the sweep efficiency shown in Table 5.

Conclusions

The proposed multi-Gaussian pore-throat-size decomposition presents significant benefits when compared to Thomeer's method (1960). Thomeer method uses the entry-pressure P_d as an adjusting parameter, whereas in our method we may choose to preserve the observed P_d instead of using it as a fitting parameter. The multi-Gaussian decomposition parameters: $r_{mode\,i}$; σ_i; $r_{d\,i}$; $r_{\min i}$ and x_i have a clear physical and statistical meaning. Such decomposition parameters may be easier to upscale and correlate to other core and well log measurements, e.g. NMR, sonic and dielectric logs.

Considering the truncation of the pore-throat-size distribution (the maximum r_d and the minimum pore-throat-radii r_{min}) is important to model the physical and experimental limits of the data during a multi-Gaussian decomposition, improving the method presented by Xu and Torres-Verdín (2013).

Our analysis of the truncated multi-Gaussian decomposition parameters show interesting correlations with rock properties, some of them confirming the correlations obtained by Xu and Torres-Verdín (2013).

The new universal J^{**}-function is useful to validate the multi-Gaussian pore-throat-size decomposition and to reconstruct capillary pressure curves from the parameters provided by such method.

The proposed methods may significantly enhance the dynamic characterization and reservoir simulation of IOR and EOR in complex carbonate reservoirs, like the CO2/WAG injection to be applied to the Brazilian pre-salt reservoirs.

Overlooking the rock-pore-space geometry and network topology may result in significant errors in reservoir characterization and simulation processes. Our sensitivity study supplements the sensitivity study presented by Ferreira et al. (2015), showing a significant impact of the variability of pore-throat-size distribution on oil in place and reserves estimates for IOR / EOR processes in typical complex carbonate reservoirs, such as the ones found in the Brazilian Pre-Salt.

Missing the mean values of the parameters of the multi-Gaussian pore-throat-size decomposition during the SCAL sampling, particularly if their variability is high, may result in huge impacts on OOIP and ultimate reserves. Therefore, SCAL results should be corrected according to such parameters mean values obtained from MICP or well log data. Furthermore, such results should also be adjusted to high-quality water-saturation logs in order to build a suitable reservoir SHM.

Nomenclature

Abbreviations

API	=	*API fluid density*
CDF	=	*cumulative distribution function*
DRRT	=	*dynamic reservoir-rock typing*
EOR	=	*enhanced oil recovery*
FZI	=	*flow-zone indicator*
IOR	=	*improved oil recovery*

MICP = *mercury-injection capillary pressure*
NMR = *nuclear magnetic resonance*
OOIP = *original volume of oil in place*
Np = *cumulative oil production*
PDF = *probability-density function*
RQI = *reservoir-quality index*
*RQI** = *proposed dynamic reservoir-rock-typing index*
SCAL = *special core analysis*
SHM = *saturation height model*
WAG = *water-alternating-gas injection*
WWRC = *joint-industry worldwide rock catalog*

Symbols

k = *absolute permeability*
ϕ_e = *effective porosity*
R_{35} = *pore-throat radius corresponding to the capillary pressure at 35% of mercury saturation*
$R_{inflection}$ = *pore-throat size corresponding to inflection of the capillary pressure curve*
P_c = *capillary pressure*
γ = *fluids' interfacial tension*
θ = *rock-fluids-contact angle*
r_{throat} = *pore-throat radius*
τ_h = *hydraulic tortuosity*
B_v = *volume fraction of the injected mercury to the total sample's bulk volume*
B_∞ = *bulk volume percentage occupied by mercury at the maximum applied pressure*
G = *Thomeer's pore geometrical factor*
P_d = *displacement (entry) capillary pressure*
S_w = *wetting-fluid saturation (air for MICP, water for water-wet conditions)*
S_{wirr} = *Irreducible water saturation*
S_{wmin} = *minimum wetting-fluid saturation*
S_{wmax} = *maximum wetting-fluid saturation*
S_w^* = *normalized wetting-fluid saturation*
S_{Hg} = *mercury (non-wetting-fluid) saturation*
ζ = *non-truncated saturation function of the pore-throat radius*
x_j = *volume fraction corresponding to a pore-throat radius Gaussian component*
α = *ratio between RQI* for the first and second pore systems*
BI = *Ashman and Wang bimodality index*
J = *Leverett J-function*
J^* = *El-Khatib (1995) modified Leverett J-function*
J^{**} = *Proposed universal J-function*
J_{mG}^{**} = *Proposed universal multi-Gaussian J-function*
k^* = *modified absolute permeability*
T_M = *simulation transmissibility multiplier*
T_M^* = *modified transmissibility multiplier*
μ = *Mean value of a probability distribution*
σ = *standard deviation of a probability distribution*
r_{mode} = *Mode value of a pore-throat-radius probability distribution*
σ_v = *matrix-to-connected-vugs transmissibility / diffusivity volumetric coefficient*

$l_{x,y,z}$ = *matrix block dimensions in dual porosity systems*
M = *mobility ratio between the displacing and displaced fluids*
P_{sat} = *pressure at saturation point*
B_{oi} = *oil formation volume factor*
μ_{oi} = *oil viscosity*
R_{si} = *dissolved gas-oil ratio*
r_{min} = *Minimum pore-throat radius of a corresponding distribution*
R_d, r_d = *Maximum pore-throat radius corresponding to the entry capillary pressure*

Conversion Factors

All equations are presented considering the use of a consistent unit system. If a field-unit system is used then proper conversion factors should be applied.

Acknowledgements

The authors would like to acknowledge the Schlumberger Brazil Research and Geoengineering Center management, petrophysics, and reservoir engineering program teams.

References

Abramowitz, M. and Stegun, I. A., (1972), Handbook of Mathematical Functions with Formulas, Graphs, and Mathematical Tables. New York: Dover Publications, ISBN 978-0-486-61272-0, http://www.nr.com/aands/

Al-Kharusi, A.S., Blunt, M.J., 2007. Network Extraction from Sandstone and Carbonate Pore Space Images. Journal of Petroleum Science and Engineering 56-4, 219 – 231.http://dx.doi.org/10.1016/j.petrol.2006.09.003

Amaefule, J. O., Altunbay, M., Tiab, D., Kersey, D. G., & Keelan, D. K., 1993. Enhanced Reservoir Description: Using Core and Log Data to Identify Hydraulic (Flow) Units and Predict Permeability in Uncored Intervals/Wells. Presented at SPE Annual Technical Conference and Exhibition, 3-6 October, Houston, Texas. SPE-26436-MS. http://dx.doi.org/10.2118/26436-MS.

Souza, A., Machado, V., Coutinho, B., Trevizan, W., Rios, E., Bagueira, R., Carneiro, G., Boyd, A., Zielinski, L., Polinski, R., Hurlimann, M., Schwartz, L., 2013, Permeability Prediction Improvement Using 2D NMR Diffusion T2 Maps, , SPWLA Annual symposium, in New Orleans, June 23-27, 2013.

Arns, J.-Y. and Robins, V. and Sheppard, A.P. and Sok, R.M. and Pinczewski, W.V. and Knackstedt, M.A., 2004. Effect of Network Topology on Relative Permeability. Transport in Porous Media 55-1, 21–46. http://dx.doi.org/10.1023/B:TIPM.0000007252.68488.43

Ashman, K.M. and Bird, C.M. and Zepf, S.E., 1994, Detecting Bimodality in Astronomical Datasets. Astronomical Journal, v.108-6, p. 2348-2361

Bize-Forest, N., Baines, V., Boyd A., Moss A., Oliveira R., 2014. Carbonate Reservoir Rock Typing and the Link between Routine Core Analysis and Special Core Analysis. Presented at the International Symposium of the Society of Core Analysts, 8-11 September, Avignon, France, SCA2014-A057

Bize-Forest N., Centeno R., Bize E., Polinski R, Boyd A., Oliveira R., He A., Le Nir I., 2014. Vug Porosity Estimation using Acoustic Images in Oil or Water-based Mud Systems. Paper BG09, EAGE Dubai, Oct 13-16, 2014

Brie. A, Johnson, D.L. and Nurmi, R.D., 1985. Effect of Spherical Pores on Sonic and Resistivity Measurements. Presented at the 26th Annual Logging Symp., Houston, TX. SPWLA, 1985.

Buiting, J.J.M. and Clerke, E.A., 2013. Permeability from Porosimetry Measurements: Derivation for a Tortuous and Fractal Tubular Bundle. Journal of Petroleum Science and Engineering 108, 267–278. http://dx.doi.org/10.1016/j.petrol.2013.04.016

Clennell, M.B., 1997. Tortuosity: a Guide through the Maze. Geological Society Special Publication 122, 299–344. http://dx.doi.org/10.1144/GSL.SP.1997.122.01.18

Clerke, E.A. and Mueller III, H.W. and Phillips, E.C. and Eyvazzadeh, R.Y. and Jones, D.H. and Ramamoorthy, R. and Srivastava, A., 2008. Application of Thomeer Hyperbolas to Decode the Pore Systems, Facies and Reservoir Properties of the Upper Jurassic Arab D Limestone, Ghawar Field, Saudi Arabia: A "Rosetta Stone" Approach. GeoArabia 13-4, 113–160.

Clerke, E.A. and Martin, P.R. 2004. Thomeer Swanson Excel Spreadsheet and FAQ's and User Comments. Presented and distributed at the SPWLA 2004 Carbonate Workshop, Noordwijk.

Core Lab, 2014. Worldwide Rock Catalog™, http://www.corelab.com/irs/studies/wwrc (accessed 19th of June 2015)

Cosentino, L., 1992. Integrated Reservoir Studies. Editions Technip, Paris.

Dullien, F. A. L., 1979. Porous Media: Fluid Transport and Pore Structure. Academic Press, San Diego.

El-Khatib, N., 1995. Development of a Modified Capillary Pressure J-function. Presented at SPE Middle East Oil Show, 11-14 March, Bahrain, SPE-29890-MS. http://dx.doi.org/10.2118/29890-MS

Ferreira, F.C., Booth, R., Oliveira, R., SPE, Schlumberger, Carneiro, G., Bize-Forest, N., and Wahanik, H., 2015. New Rock-Typing Index Based on Hydraulic and Electric Tortuosity Data for Multi-Scale Dynamic Characterization of Complex Carbonate Reservoirs, presented at ATCE 2015, Houston, SPE-175014-MS

Hassall, J., Ferraris, P., Al-Raisi, M., Hurley, N.F., Boyd, A., and Allen, D.F., 2004: Comparison of Permeability Predictors from NMR, Formation Image and other Logs in a Carbonate Reservoir, SPE 88683 presented at the 11th Abu Dhabi International Petroleum Exhibition and Conference, Abu Dhabi, U.A.E., October 10-13, 2004.

Gurpinar , O., Kalbus , J., and List , D., 1999. Numerical Modeling of a Triple Porosity Reservoir, presented at the SPE Asia Pacific Improved Oil Recovery Conference in Kuala Lumpur, Malaysia, 25–26 October 1999. SPE 57277.

Jerry Lucia, F., 1999. Characterization of Petrophysical Flow Units in Carbonate Reservoirs: Discussion. AAPG Bulletin 83-7, 1161–1163.

Kazemi, H., Merrill JR., L. S., Porterfield, K. L., and Zeman, P. R., 1976. "Numerical Simulation of Water-Oil Flow in Naturally Fractured Reservoirs," paper SPE 5719, Society of Petroleum Engineers Journal 16, No. 6, 317-326.

Kenyon, W. E., Allen, D. F., Lisitza, N. V., & Song, Y. Q., 2002. Better Pore-Size Distributions from Stimulated-Echo NMR Lab Measurements Using Magnetic Susceptibility Contrast and Small Encoding Angles. SPWLA Symposium Transactions, SPWLA-2002-III.

Kleinberg, R. L., & Vinegar, H. J., 1996. NMR Properties of Reservoir Fluids, SPWLA, The Log Analyst, 37-6, 20-32

Klinkenberg, L.J., 1941. The Permeability of Porous Media to Liquids and Gases. American Petroleum Institute, API-41-200.

Kozeny, J., 1927. Uber die Kapillare Leitung Deswassers im Boden (Aufstieg Versickerung und Anwendung auf die Bewasserung. Sitz. Ber. Akad. Wiss,Wien, Math. Nat. (Abt. Iia) 136a, 271.

Leverett, M., 1941. Capillary Behavior in Porous Solids. SPE Trans. AIME 42-1, 152–169. SPE-941152-G. http://dx.doi.org/10.2118/941152-G

Lindquist, W.B. and Venkatarangan, A. and Dunsmuir, J. and Wong, T.-F., 2000. Pore and Throat Size Distributions Measured from Synchrotron X-ray Tomographic Images of Fontainebleau Sandstones. Journal of Geophysical Research: Solid Earth 105-89, 21509–21527.

Øren, P.E., Bakke, S., 2003. Reconstruction of Berea Sandstone and Pore-Scale Modelling of Wettability Effects. Journal of Petroleum Science and Engineering 39-3/4, 177 – 199. http://dx.doi.org/10.1016/S0920-4105(03)00062-7

Pizarro, J. O. D. S., & Branco, C. C. M., 2012. Challenges in Implementing an EOR Project in the Pre-Salt Province in Deep Offshore Brasil. Presented at SPE EOR Conference at Oil and Gas West Asia, 16-18 April, Muscat, Oman. SPE-155665-MS. http://dx.doi.org/10.2118/155665-MS

Ramakrishnan, T.S., Ramamoorthy, R., Fordham, E., Schwartz, L., Herron, M., Saito, N. and Rabaute, A., 2001. A Model-Based Interpretation Methodology for Evaluating Carbonate Reservoirs, Paper SPE 71704 presented at the SPE Annual Technical Conference and Exhibition, New Orleans, LA, USA, September 30 - October 03, 2001.

Ren, C. and Mackenzie, A.R., 2007. Closed-Form Approximations to the Error and Complementary Error Functions and Their Applications in Atmospheric Science. Atmospheric Science Letters, v. 8-3, p. 70-73. http://dx.doi.org/10.1002/asl.154

Skalinski, M., Gottlib-Zeh, S., & Moss, B., 2006. Defining and Predicting Rock Types in Carbonates - Preliminary Results from an Integrated Approach using Core and Log Data from the Tengiz Field. Society of Petrophysicists and Well-Log Analysts.

Thomeer, J.H.M. 1960. Introduction of a pore geometrical factor defined by a capillary pressure curve. Petroleum Transactions, AIME, v. 219, T.N. 2057, p. 354-358.

Wang, J., Wen, S., Symmans, W. F., Pusztai, L., & Coombes, K. R. (2009). The Bimodality Index: A Criterion for Discovering and Ranking Bimodal Signatures from Cancer Gene Expression Profiling Data. Cancer Informatics, 7, 199–216.

Washburn, E. W., 1921, Note on a Method of Determining the Distribution of Pore Sizes in a Porous Material. Proceedings of the National Academy of Science, v. 7, p. 115–116.

Xu, C., Torres-Verdín, C., 2013. Pore System Characterization and Petrophysical Rock Classification Using a Bimodal Gaussian Density Function, Math Geoscience 45, 753–771.

Xu, C., Torres-Verdín, C., 2014, Petrophysical Rock Classification in the Cotton Valley Tight-Gas Sandstone Reservoir with a Clustering Pore-System Orthogonality Matrix, SEG Technical paper